Soft Matter

PAPER

View Article Online
View Journal | View Issue

Cite this: *Soft Matter*, 2017, 13, 2995

Smart design of wettability-patterned gradients on substrate-independent coated surfaces to control unidirectional spreading of droplets†

Huaping Wu,*[ab] Kai Zhu,[a] Binbin Cao,[a] Zheng Zhang,[a] Bingbing Wu,[a] Lihua Liang,[a] Guozhong Chai[a] and Aiping Liu*[c]

Received 23rd December 2016,
Accepted 23rd March 2017

DOI: 10.1039/c6sm02864k

rsc.li/soft-matter-journal

Highly adherent wettability patterns on the substrate-independent superhydrophobic surfaces of trimethoxyoctadecylsilane modified titanium dioxide (TiO_2)-based coatings were prepared by using commercial photolithography. Three custom unidirectional channels with gradient wettability patterns were obtained by spatially selective wettability conversion from superhydrophobic to superhydrophilic when the coatings were exposed to ultraviolet light (~365 nm). The movement behavior of droplets on these unidirectional channels was studied and the displacement of droplet movement was effectively controlled. Integrating the idea of gradient wettability patterns into planar microfluidic devices (microreactors), a self-driven fluid transport was achieved to realize droplet metering, merging or reaction, and rapid transport. This self-driven fluid transport with gradient wettability patterns has great potential in fabricating a new category of pump-free microfluidic systems that can be used in various conditions.

1. Introduction

In recent years, multifunctional superhydrophobic coatings with special adhesion have attracted great attention primarily due to their potential applications in many fields,[1–5] such as self-cleaning,[6,7] droplet bouncing,[8,9] biomedical devices,[10,11] and fluidic devices.[12,13] Among them, surfaces for controlling liquid spreading behavior have been proved employable in microfluidic devices,[14–20] DNA microarrays,[21] condensation heat transfer,[22] antifogging,[23] *etc.* Hydrophilic/hydrophobic patterned surfaces[24–27] offer a means for controlling the wetting behavior of aqueous media. Unidirectional spreading of droplets[28–31] can be generally created by exploiting a wettability gradient surface, on which the droplet moves spontaneously in the direction of increasing wettability. Greenspan[32] first theoretically predicted the directional movement of droplets on a wettability gradient surface and found droplets spreading to a more hydrophilic region when the driving force provided by the wettability gradient was greater than the surface hysteresis. Chaudhury and Whitesides[33] experimentally realized the directional movement of water droplets to the hydrophilic side on wettability gradient surfaces and verified the theory of Greenspan. Since then, many similar studies have been carried out. For example, Gu *et al.*[34] investigated the movement behavior of droplets on a surface with gradient microstructure, and found a necessary condition for the spontaneous movement of the droplets (namely the transition of the droplets from the Cassie–Baxter (CB) state to the Wenzel state). Lugli *et al.*[35] prepared surfaces with chemical gradients using the pulling method, and realized the directional movement of droplets with a speed of 5 mm s^{-1}. Chandesris *et al.*[36] obtained quicker flow velocity and longer flow distance for droplets by constructing surfaces with microstructure and chemical constituent gradients. Bliznyuk *et al.*[37] carried out a detailed experimental study of glycerol/water mixture droplets over chemically defined linear-stripe-patterned surfaces and verified the dependence of droplet velocities on the length and relative hydrophobicity of the patterns. Although there have been a large number of studies related to gradient wetting surfaces[37–40] and movement behaviors of droplets both experimentally and theoretically,[41–44] only a few wettability gradient surfaces are substrate-independent,[45] and the distance of droplet movement is still hard to control quantitatively due to the uncontrollability of gradient micro–nano structure or chemical constituents.

Wettability patterns as a good way to strictly control chemical constituents owing to the significant difference in wettability have been applied in many fields, such as the controlling of liquid shape and size,[46,47] nanoliter-sized droplet deposition,[48] selective reproduction of control cells[49–51] used in biological engineering,[52,53] microfluidic devices,[54,55] and water collection.[56]

[a] Key Laboratory of E&M (Zhejiang University of Technology), Ministry of Education & Zhejiang Province, Hangzhou 310014, China. E-mail: wuhuaping@gmail.com
[b] State Key Laboratory of Structural Analysis for Industrial Equipment, Dalian University of Technology, Dalian 116024, China
[c] Center for Optoelectronics Materials and Devices, Zhejiang Sci-Tech University, Hangzhou 310018, China. E-mail: liuaiping1979@gmail.com

† Electronic supplementary information (ESI) available. See DOI: 10.1039/c6sm02864k

Various methods and technologies have been developed to prepare wettability patterns on superhydrophobic surfaces such as plasma treatment,[57–60] photo-induced modification,[61] soft-lithography,[62] and ink printing.[63] However, these methods involve complicated preparation processes, expensive equipment and substrate-dependent problems. Assuming that a gradient pattern was introduced in the wettability surface, the self-driven transport of droplets could be realized to control the flow direction and length. In this study, highly adherent wettability patterns are fabricated on the surfaces of various substrates by using titanium dioxide (TiO_2) nanoparticle coatings modified with trimethoxyoctadecylsilane (TMOS) *via* photolithography. Three custom unidirectional channels with gradient striped wettability patterns are prepared. The movement behavior and displacement of droplets are effectively controlled by designing the corresponding wettability gradient. Furthermore, the idea of gradient wettability patterns is integrated into planar microfluidic devices (microreactors) to self-driven fluid transport for realizing droplet metering, merging or reaction, and rapid transport.

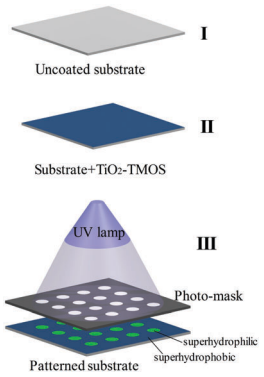

Fig. 1 Fabrication process of a patterned surface: (I) uncoated substrate (glass, dustless cloth or filter paper), (II) spin-coating of a TMOS–TiO_2 ethanol suspension on the substrates, (III) UV treatment of the superhydrophobic substrate through a patterned photomask (top) to form superhydrophilic regions (bottom). Exposed regions turned superhydrophilic upon 30 min exposure to UV radiation, while the unexposed regions remained superhydrophobic.

2. Experimental

Chemicals and materials

TMOS (Aladdin), TiO_2 nanoparticles (anatase and rutile, $<$40 nm, 99.7% trace, Sigma Aldrich) and ethanol ($\sim$99 wt%, Eagle Chemical Reagent Co., Ltd, Zhejiang) were of analytical grade and were used without further purification. TiO_2 nanoparticles showed micro- and nanoscale roughness which was helpful in promoting the photocatalytic degradation of hydrophobic chemistries on them upon exposure to UV radiation. The deionized water used in the synthesis was obtained from a Millipore Q purification system (resistivity $>$ 18 MΩ cm). Four kinds of substrates were used, namely a 2 mm-thick glass plate, a transparent polyethylene terephthalate (PET) film (for photomask fabrication using a high-resolution laser printer), dustless cloth and filter paper. All of the above materials were readily available in the marketplace.

Experiment and characterization

Wettability-patterned coatings were prepared *via* a facile and scalable approach (Fig. 1). Briefly, a uniform mixture of 0.2 mL of TMOS, 0.1 g of TiO_2 nanoparticles and 10 mL of ethanol was spin-coated onto a glass substrate several times (three-step spin procedure includes 500 rpm min^{-1} for 10 s, 1000 rpm min^{-1} for 5 s and 500 rpm min^{-1} for 5 s) and dried in a preheated oven at 100 °C for 1 hour, forming a superhydrophobic surface. For flexible substrates like dustless cloth or filter paper, superhydrophobic surfaces were obtained by soaking them in a uniform mixture of TMOS, TiO_2 nanoparticles and ethanol for 30 minutes. After that, the flexible substrates were dried in a preheated oven at 100 °C for 1 hour to improve the adhesion of TMOS–TiO_2 onto the substrates. Superhydrophilic patterns were formed on these superhydrophobic surfaces through selectively exposing the substrates to UV radiation (250 W, 365 nm) for 30 minutes by using a PET photomask with black negative patterns. Complex pattern designs with features as fine as 20 μm were obtained when decomposed TMOS became hydrophilic under TiO_2-assisted photocatalysis with UV light irradiation.

The morphology of the sample surface was observed by scanning electron microscopy (SEM, Hitachi S4800). The crystalline phases of the samples were characterized by X-ray diffraction (XRD) using a conventional diffractometer (Bruker AXS D8) with an area detector operating under a voltage of 40 kV and a current of 40 mA using Cu Kα radiation (λ = 0.15418 nm). X-ray photoelectron spectroscopy (XPS, Kratos AXIS Ultra DLD) was used to track the modification and decomposition of TMOS. The compositions and structures of the samples before and after irradiation were analyzed using infrared (IR) spectra (Thermo, Nicolet 6700) and Raman spectra (Thermo Fisher DXR Raman spectrometer using a He–Ne laser, λ = 632.8 nm). The water contact angle (CA, θ) was measured using 4 μL droplets of deionized water with a contact angle instrument (Thermo, DCA-322) with reference to some related works.[64–66] A high-speed camera was used to capture rapid events, such as directional liquid spreading, merging and rapid transport. The water drops were dispensed using a syringe pump through a needle with 100 μm inner diameter.

3. Results and discussion

Microstructure of the TMOS–TiO_2-coated substrate

Fig. 2 shows the morphology of the TMOS–TiO_2 coated substrate before and after irradiation. The conglomeration of nanoparticles with roughness ranging from a few hundreds of nanometers to a few tens of microns can be found before irradiation (Fig. 2a) because of the TMOS modification on the TiO_2 nanoparticle surfaces. When the TMOS was decomposed after UV irradiation, lower roughness was presented due to the original feature of the TiO_2 nanoparticles (Fig. 2b). The TMOS–TiO_2 coating with a thickness of about 5 μm (Fig. 2c) shows a good superhydrophobic behavior with a static water CA of about 152.0° (the inset in Fig. 2a), and a small CA hysteresis (which is discussed in detail later).

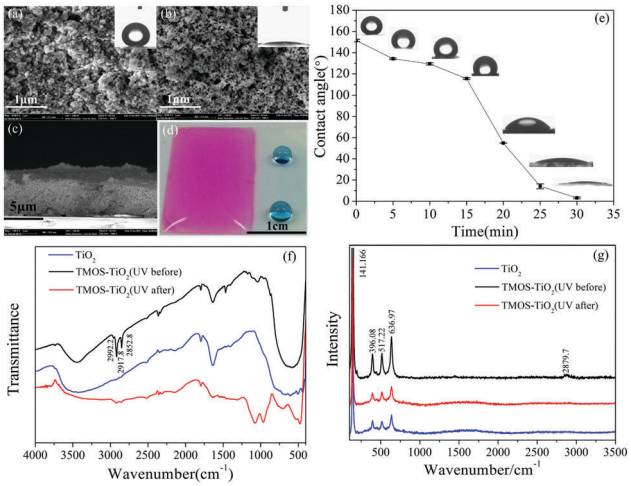

Fig. 2 Top view of scanning electron microscopy images of TMOS–TiO_2 layers on a glass substrate (a) before and (b) after UV treatment. The insets show the photographs of water droplets deposited on the substrates. (c) Cross-sectional view of TMOS–TiO_2 layers on the glass substrate after UV treatment. (d) Striking contrast when a droplet is placed in superhydrophilic and superhydrophobic regions, respectively. (e) Water contact angles of TMOS–TiO_2 coating on the glass substrate as a function of UV treated time. (f) IR and (g) Raman spectra of the TiO_2 and TMOS–TiO_2 coatings before and after UV irradiation for 30 minutes.

This dominant superhydrophobicity mode of the surface may be assigned to the Cassie model because of the micron and submicron roughnesses. The influences of TMOS concentration and the number of spin coatings on water CAs were also analyzed. A 2.0% concentration ($V_{TMOS}/V_{ethanol}$) for TMOS and 5 times spin are sufficient for obtaining a stable superhydrophobic surface (Fig. S1 and S2, ESI†), and therefore are chosen in the subsequent experiments. When the TMOS was decomposed, the sample surface becomes superhydrophilic (the inset in Fig. 2b), with the CA ranging from 0° to 5° by repeated measurements. A striking contrast was observed, with the droplet either nearly spherical in shape in the superhydrophobic region or spread completely in the superhydrophilic one (Fig. 2d). The variation of the static water CAs of the TMOS–TiO_2-coated surface with respect to UV illumination time is also shown, with the CAs gradually decreasing from 152.0° to nearly zero (<5°) with increase in illumination time to 30 minutes and becoming stable ultimately (Fig. 2e). The dramatic decrease of the CA during 15–25 minutes might be attributed to the obvious increase in the oxygen vacancies produced by photogenerated holes, which could adsorb more water molecules in the air and therefore result in the enhancement of the hydrophilicity of the coating surface.[67–69] Additionally, the aggregated droplet could infiltrate into the gap between the micro–nano structures, leading to the transition of the wetting regime of the droplet from the Cassie state to the Wenzel state.[70–73] This wettability conversion can be attributed to the decomposition of alkyl chains of TMOS adsorbed on the TiO_2 surfaces by the UV-assisted dissociation of ozone photogenerated in air (reaction mechanism shown in Fig. S3, ESI†) and was further examined using IR and Raman spectra. The new absorption peaks at 2992.2 cm^{-1}, 2917.8 cm^{-1} and 2852.8 cm^{-1} in the IR spectra correspond to the vibrations of long-chain alkyl $-CH_3$ and $-CH_2$,[74] indicating the successful modification of TMOS on the TiO_2 surfaces. After UV irradiation, the peaks related to $-CH_3$ and $-CH_2$ vibrations almost disappear, meaning the alkyl chain decomposition (Fig. 2f). This could further be confirmed using Raman spectra (Fig. 2g) due to the disappearance of the $-CH_2$ peak at 2879.7 cm^{-1} after UV irradiation.[61] The chemical compositions of the TMOS-coated surfaces were determined through XPS measurements before and after UV irradiation. The atomic concentration of C decreases from 49.3% to 11.1% due to the decomposition of the alkyl chains of the TMOS layers on the TiO_2 nanoparticles (Table S1, ESI†). The peak intensities related to O, Si and Ti elements increase after UV illumination (Fig. S4a–c, ESI†) because of more TiO_2 exposure. The ratios associated with C–O (286.5 eV) and C=O (288.7 eV) bonds obviously increase after alkyl chain decomposition (Fig. S4d, ESI†). XRD results show that UV irradiation does not affect the crystalline phases of the TMOS–TiO_2 surfaces (Fig. S5, ESI†).

Droplet manipulation on substrate-independent wettability-patterned surfaces

The TMOS–TiO_2-coated superhydrophobic surfaces are substrate-independent and can be formed on various substrates, such as a glass sheet (rigid substrate, water CA is 152.5°, Fig. 3a), dustless cloth (flexible substrate, water CA is 156.2°, Fig. 3b) and filter paper (flexible substrate, water CA is 159.1°, Fig. 3c). We also tested the sliding behaviors of a droplet on these TMOS–TiO_2-coated substrates. The sliding angles (SAs) on the TMOS–TiO_2-coated glass sheet and dustless cloth are 3.0° (Fig. S6a, ESI†) and 2.9° (Fig. S6b, ESI†), respectively. However, for the TMOS–TiO_2-coated filter paper, we could hardly deposit a droplet on a specific area because the droplet easily rolled away when it touched the surface; hence we didn't obtain the specific SA (Fig. S6c, ESI†). It is generally accepted that the SA is less than 5° for this kind of situation.[75] Moreover, the advancing and receding contact angles (ACAs and RCAs) of the droplets on the surfaces of the TMOS–TiO_2-coated glass sheet, dustless cloth and filter paper are 153.5° and 151.2°, 157.2° and 155.1°, and 159.6° and 158.7°, respectively, indicating that all of these surfaces have ultralow

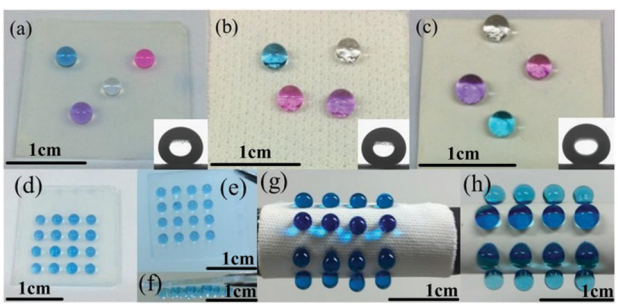

Fig. 3 Images of spherical water droplets placed on various TMOS–TiO_2-coated substrates: (a) glass, (b) dustless cloth and (c) filter paper. The insets are the CA images of water droplets. (d–f) A 4 × 4 array of 6 μL droplets stored on various TMOS–TiO_2-coated substrates: glass surfaces with (d) 0°, (e) 90° and (f) 180° tilts; curly flexible substrates including (g) dustless cloth and (h) filter paper.

CA hysteresis. Besides, we chose the TMOS–TiO_2-coated glass sheet as a representative sample and tested the CAs of water droplets every four days for a month (Fig. S7, ESI†), which revealed the long-term stability of TMOS–TiO_2-coated surfaces. The switchable wetting control and patterning *via* TMOS–TiO_2 coating could realize the manipulative actions of droplets, including storage and visible superhydrophilic patterns on the superhydrophobic surface by depositing colored droplets. For example, a 4 × 4 droplet array (individual droplet size of 6 μL for more clear observation) could be cast on the coated glass surface (Fig. 3d) and remain stable even at tilt angles of 90° (Fig. 3e) and 180° (Fig. 3f), and also be formed on curly flexible substrates (dustless cloth in Fig. 3g and filter paper in Fig. 3h), indicating sufficient adhesion between the droplets and coated surfaces. Other visible patterns with different sizes and geometries are also shown in Fig. S8 (ESI†).

Unidirectional spreading of droplets

When superhydrophilic/superhydrophobic micropatterns are gradient changeable, a wettability gradient will be achieved. We chose the stripe-patterned gradient surfaces because the striped patterns create a preferential direction for liquid spreading parallel to the stripes and confine motion to the perpendicular direction, resulting in anisotropic wetting properties.[37,76–80] By designing the photomask properly, we obtained three custom unidirectional channels with gradient wettability patterns, as shown in Fig. 4a. The width W and length L of the channels are 2 mm and 8 mm, respectively, where the wettability gradient direction is from left to right (the superhydrophobic units are stripes with a width w_0 of 20 μm and length l_0 of 1 mm, every channel is divided into eight areas, and the spacing P between two adjacent stripes increases from left (initial 40 μm) to right with a ΔP increment). We determined the wettability-patterned gradient ($\Delta = \Delta P/w_0$, the ratio of the superhydrophilic area increment to superhydrophobic area along the wettability gradient) on the three channels to be 1, 1.5 and 2, respectively (Fig. 4a). The CAs,

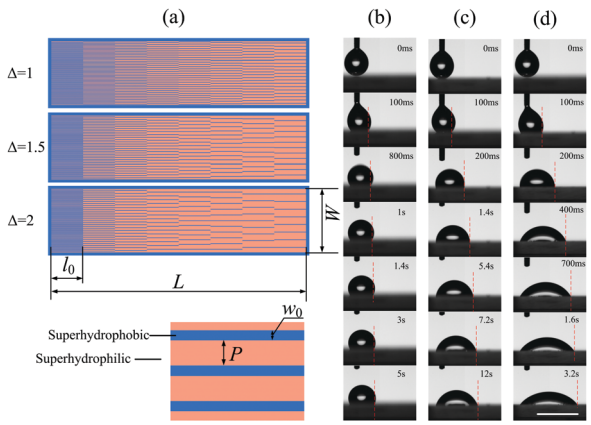

Fig. 4 (a) Three examples of unidirectional channels designed on a photomask. Blue and orange colors represent superhydrophobic and superhydrophilic regions, respectively. (b), (c) and (d) Time-lapsed images of water droplet transport through these three unidirectional channels, respectively. The scale bars for all figures are 5 mm.

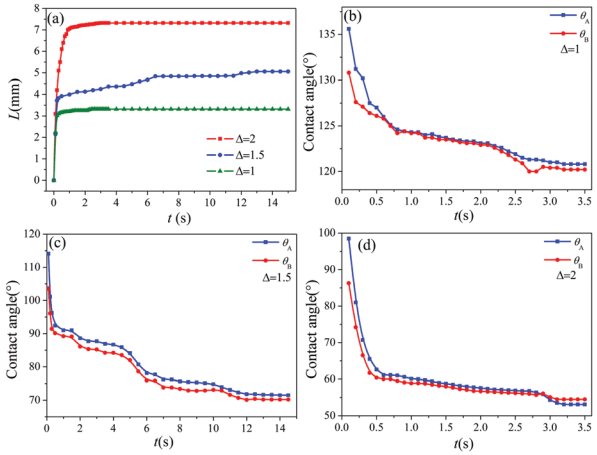

Fig. 5 (a) Evolution of droplet displacement as a function of time – dynamic contact angle θ_A (left of the droplets) and θ_B (right of the droplets) as a function of time: (b) Δ = 1; (c) Δ = 1.5; and (d) Δ = 2.

ACAs and RCAs on each area of these three channels are shown in Fig. S9 (ESI†). When a water droplet is placed gently in the left end of the channel, the droplet could spread rapidly along the direction of the wettability gradient without any external stimulus. The time-lapsed images of the transport of water droplets through these three unidirectional channels are shown in Fig. 4(b–d), giving drop displacements of 3.32 mm, 5.06 mm and 7.35 mm (Fig. 5a), respectively. The receding edge is pinned due to the strong adhesion in the patterned surface, and the advancing side of the droplet moves because of the wettability gradient, as shown in Fig. 4(b–d). The changes in the dynamic contact angles θ_A (left of the droplets) and θ_B (right of the droplets) in the process of droplet movement are shown in Fig. 5(b–d). The θ_A decreases from 135.6° to 120.8°, 114.1° to 71.5° and 98.5° to 53.1° on the three unidirectional channels, respectively, while the θ_B decreases from 130.8° to 120.2°, 103.6° to 70.2° and 96.3° to 54.5°, respectively, indicating the spreading of droplets.

Based on the above experimental results, we theoretically analyzed the process of droplet movement. For a thin strip of liquid thickness dy parallel to the spreading direction (Fig. 6), the wettability gradient driving force (F_D) at the k location which drives the droplet toward a more wettable region of the surface can be described as[33,37,38,81]

$$F_D = 2R\gamma_{LV}\sum_{n=1}^{k}(\cos\theta_n - \cos\theta_{n-1}), \quad (1)$$

where R is the base radius of the droplet to contact the surface in the y direction just before unidirectional spread, and γ_{LV} is the

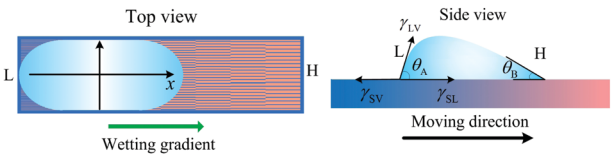

Fig. 6 Schematic of a droplet on a wettability gradient surface. The wettability changes from hydrophobic (low γ_{SV}) to hydrophilic (high γ_{SV}).

surface tension of the droplet. θ_n corresponds to the CA of the droplet on the nth wettability pattern of one channel. The detailed derivation is provided in Part II in the ESI.† The hysteresis force (F_H), due to CA hysteresis, is always opposite to the moving direction and can be expressed as[33,37,38,81,82]

$$F_H = 2R\gamma_{LV}\sum_{n=1}^{k}\int_0^{\frac{\pi}{2}}(\cos\theta_{rn} - \cos\theta_{an})\cos\phi \mathrm{d}\phi = 2R\gamma_{LV}\sum_{n=1}^{k}(\cos\theta_{rn} - \cos\theta_{an}). \quad (2)$$

Here, θ_{an} and θ_{rn} correspond to the ACAs and RCAs on the nth wettability pattern of one channel. The motion of the droplet is also hindered by viscous drag, referred to as the friction force F_η.[37,81–84] It has been reported that the estimated viscous drag is orders of magnitude smaller than the F_D.[37,85] Therefore, we ignore the effect of viscous drag. Actually, the process of spontaneous spreading of the droplet should be a cumulative process of F_D and F_H, so we calculated the F_D and F_H of the three kinds of channels in different positions (Fig. 7a–c). By comparing F_D and F_H, we can determine whether the droplet could spread unidirectionally or not. When F_D overpowers F_H, the droplet can spread along the direction of the wettability gradient, while the droplet would be pinned when F_D is below F_H. The position of F_D equal to $F_H(P_c)$ has been found to be located in the ranges of 3–4 mm, 5–6 mm and 7–8 mm, respectively, which can well explain the displacements of droplet movement on the three unidirectional channels (Fig. 4(b–d)). Note that the mechanics criterion can only determine the scope of estimates due to the error of measuring CAs and inertia of water movement. Therefore, the flow direction and displacement of droplet movement can be elaborately designed and effectively controlled by modulating the density and orientation of gradient wettability patterns, which might be hailed as intelligent. Since the fabrication of gradient wettability patterns is substrate-independent, the method is universal.

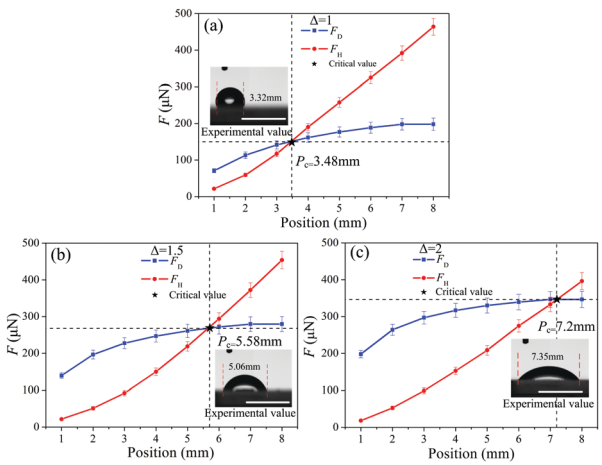

Fig. 7 Wettability gradient force (F_D) and hysteresis force (F_H) at different positions on unidirectional channels with different wettability gradients: (a) Δ = 1; (b) Δ = 1.5; and (c) Δ = 2. The scale bar is 5 mm.

Droplet metering, merging and rapid transport

The idea of wettability gradients obtained by the design of gradient patterns can be integrated into microfluidic devices to achieve the goals of self-driven fluid transport. Three channels with wettability gradients are included in our design, as shown in Fig. 8. The superhydrophobic units are stripes with a width w_0 of 20 μm and length l_0 of 1 mm, and the spacing P between two stripes increases from top to bottom. Channels A and B are 10 mm long and 1 mm wide, spaced parallel to each other at an axis-to-axis pitch of 2 mm. Channel C is 12.5 mm long with a circular storage area of the droplet in the terminal, and the start of Channel C is designed as a wedge-shaped structure and protrudes between Channels A and B to facilitate the liquid draining process. Region D is used to collect liquid. Water droplets were dispensed one at a time using metering syringes strictly placed over the starts of Channels A and B at a very low altitude; therefore, the drops fell at a low speed and the inertial effects remained negligible. The entire observation system of drop motion is illustrated in Fig. 9. Liquid transport, bridging and draining were carried out according to the following procedure. When a droplet was added to Channel B using a pipette, it spread rapidly along the direction of the wettability gradient (Fig. 10a and b). The same phenomenon could also be observed in Channel A with the addition of the same droplet (Fig. 10c and d). With the continuous dispensing of droplets, the bulges could be found (Fig. 10e). When the two bulges touched at their largest girth, the liquid bridge occurred by the merger of the bulges (Fig. 10f). The bridge grew immediately due to coalescence of the two volumes and then kept expanding axially due to the inertial effect[86] when it ultimately touched the wedge-shaped end of Channel C. The Laplace pressure gradient provided by the wedge could drive the droplets to move on, and then this process of droplet movement driven by the wettability

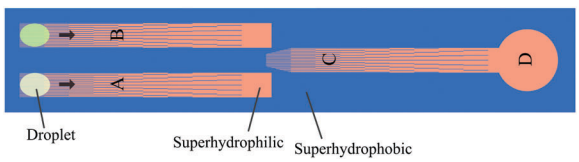

Fig. 8 Example of a multistep functional surface capable of performing pumpless liquid bridging and draining.

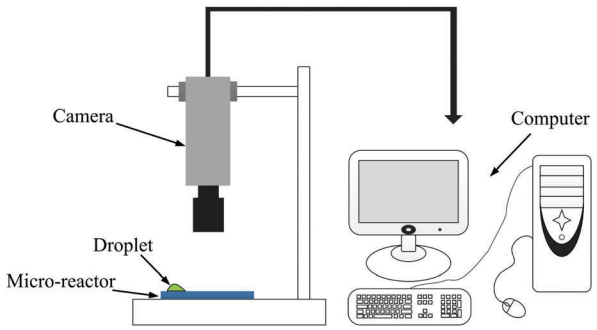

Fig. 9 The experimental setup for recording droplet movement.

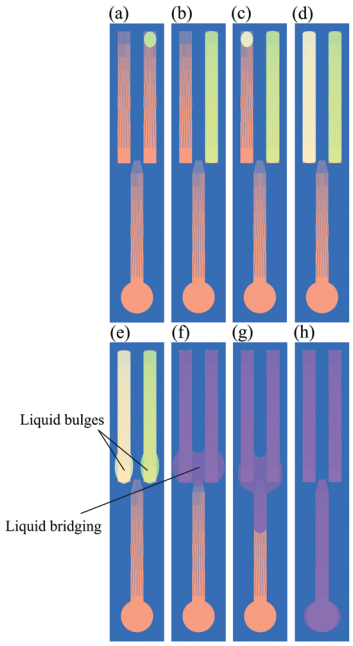

Fig. 10 Schematic illustration of liquid bridging and draining.

gradient was continued (Fig. 10g). The droplets mixed completely in Channel C (violet mixture) until they reached the designated position D (Fig. 10h). Time-lapsed images of liquid transport, bridging and draining are also shown in Fig. 11. The droplets were mixtures of water and ethanol (V_{water} : $V_{ethanol}$ = 3 : 1). And droplets placed on Channel A and Channel B were dyed with Sudan red and methylene blue, respectively. The total volume of the droplets when two bulges of the droplets touched at their largest girth was 66 μL. Note that the critical volume at which the liquid bridge occurs depends on the geometrical features of the channels and their transverse spacing. The experimental results of different concentration mixtures (V_{water} : $V_{ethanol}$ = 2 : 1 and V_{water} : $V_{ethanol}$ = 4 : 1) are also shown in Fig. S10a and b (ESI†), respectively. By comparison, we find that the speed of liquid spontaneous spreading and draining is faster for the concentration mixture (V_{water} : $V_{ethanol}$ = 2 : 1) owing to the lower surface tension. Additionally, our microfluidic device can be highly reusable. This provides an ingenious design to control droplet merging with precise volume for certain interactions or functionalities.

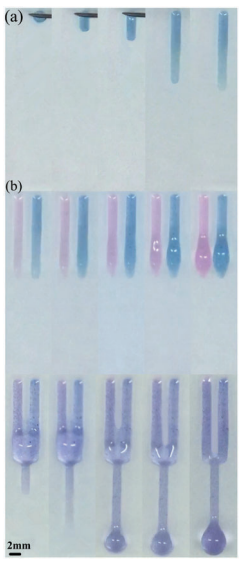

Fig. 11 (a) Time-lapsed images of droplet transport through a unidirectional channel. (b) Time-lapsed images of merging and rapid transport of two kinds of droplets with different dyes. The scale bar is 2 mm.

4. Conclusions

In conclusion, substrate-independent superhydrophobic surfaces were prepared by using TMOS-modified TiO_2 nanoparticle coatings and patterned with wettability gradients by photolithography. Then three custom unidirectional channels with highly adherent wettability patterns were elaborately designed with different wettability-patterned gradients (Δ = 1, 1.5 and 2). The movement displacements of droplets on these three channels were 3.32 mm, 5.06 mm and 7.32 mm, respectively, by controlling the density and orientation of gradient wettability patterns, which could also be confirmed by our theoretical analysis. The idea of gradient wettability patterns was further integrated into planar microfluidic devices (microreactors) to achieve the goals of self-driven fluid transport. Droplet metering, merging or reaction, and rapid transport were realized without external power sources, tube connections and expensive materials. Our result provides an ingenious design for fabrication of gradient wettability patterns, which could have great potential as pump-free microfluidic systems for droplet merging with precise volume for certain interactions or functionalities.

Acknowledgements

This work was supported by the National Science Foundation of China (Grant No. 11372280, 11672269, 51572242, 51675485), the Zhejiang Provincial Natural Science Foundation of China (Grant No. LY16E020011, LY15E050016), the Zhejiang Provincial Public Welfare Technology Application Research Projects (Grant No. 2016C31041) and the Open Research Fund Program of State Key Laboratory of Structural Analysis for Industrial Equipment, Dalian University of Technology (Grant No. GZ15205).

References

1 M. Liu, Y. Zheng, J. Zhai and L. Jiang, *Acc. Chem. Res.*, 2010, **43**, 368–377.
2 T. Darmanin, E. de Givenchy, S. Amigoni and F. Guittard, *Adv. Mater.*, 2013, **25**, 1378–1394.
3 H. Bellanger, T. Darmanin, E. de Givenchy and F. Guittard, *Chem. Rev.*, 2014, **114**, 2694–2716.
4 X. Zhang, F. Shi, J. Niu, Y. Jiang and Z. Wang, *J. Mater. Chem.*, 2008, **18**, 621–633.
5 M. Paven, P. Papadopoulos, S. Schottler, X. Deng, V. Mailander, D. Vollmer and H. Butt, *Nat. Commun.*, 2013, **4**, 2512.

6 L. Yao and J. He, *Prog. Mater. Sci.*, 2014, **61**, 94–143.
7 Y. Lu, S. Sathasivam, J. Song, C. Crick, C. Carmalt and I. Parkin, *Science*, 2015, **347**, 1132–1135.
8 J. Bird, R. Dhiman, H. Kwon and K. Varanasi, *Nature*, 2013, **503**, 385–388.
9 Y. Liu, L. Moevius, X. Xu, T. Qian, J. Yeomans and Z. Wang, *Nat. Phys.*, 2014, **10**, 515–519.
10 N. F. Huang, E. S. Lai, A. J. Ribeiro, S. Pan, B. L. Pruitt, G. G. Fuller and J. P. Cooke, *Biomaterials*, 2013, **34**, 2928–2937.
11 Y. Lai, L. Lin, F. Pan, J. Huang, R. Song, Y. Huang, C. Lin, H. Fuchs and L. Chi, *Small*, 2013, **9**, 2945–2953.
12 J. Timonen, M. Latikka, L. Leibler, R. A. Ras and O. Lkkala, *Science*, 2013, **341**, 253–257.
13 M. Hancock, K. Sekeroglu and M. Demirel, *Adv. Funct. Mater.*, 2012, **22**, 2223–2234.
14 S. Feng, S. Wang, L. Gao, G. Li, Y. Hou and Y. Zheng, *Angew. Chem., Int. Ed.*, 2014, **53**, 6163–6167.
15 G. Zhang, X. Zhang, M. Li and Z. Su, *ACS Appl. Mater. Interfaces*, 2014, **6**, 1729–1733.
16 O. Bliznyuk, J. R. Seddon, V. Veligura, E. S. Kooij, H. J. Zanvliet and B. Poelsema, *ACS Appl. Mater. Interfaces*, 2012, **4**, 4141–4148.
17 T. Wang, H. Chen, K. Liu, S. Wang, P. Xue, Y. Yu, P. Ge, J. Zhang and B. Yang, *ACS Appl. Mater. Interfaces*, 2015, **7**, 376–382.
18 Y. Hou, B. Xue, S. Guan, S. Feng, Z. Geng, X. Sui, J. Lu, L. Gao and L. Jiang, *NPG Asia Mater.*, 2013, **5**, e77.
19 T. Yasuda and S. Harada, *Twelfth International Conference on Miniaturized Systems for Chemistry and Life Sciences*, San Diego, California, USA, October 12–16, 2008.
20 Y. Nakashima, Y. Nakanishi and T. Yasuda, *Rev. Sci. Instrum.*, 2015, **86**, 015001.
21 D. Xia, J. Yan and S. Hou, *Small*, 2012, **8**, 2787–2801.
22 S. Daniel, M. K. Chaudhury and J. C. Chen, *Science*, 2001, **291**, 633–636.
23 D. Xia, L. M. Johnson and G. P. López, *Adv. Mater.*, 2012, **24**, 1287–1302.
24 K. Tadanaga, J. Morinaga, A. Matsuda and T. Minami, *Chem. Mater.*, 2000, **12**, 590–592.
25 T. Yasuda, K. Suzuki and I. Shimoyama, *7th International Conference on Miniaturized Chemical and Biochemical Analysts Systems*, Squaw Valley, California USA, October 5–9, 2003.
26 H. S. Khoo and F. G. Tseng, *International Conference on Microtechnologies in Medicine & Biology*, 2006, pp. 273–276.
27 T. Yasuda, J. Nakamura, K. Nakayama and M. Yamanaka, *16th International Conference on Miniaturized Systems for Chemistry and Life Sciences*, October 28–November 1, Okinawa, Japan, 2012.
28 K. Chu, R. Xiao and E. Wang, *Nat. Mater.*, 2010, **9**, 413–417.
29 H. Chen, P. Zhang, L. Zhang, H. Lu, Y. Jiang, D. Zhang, Z. Han and L. Jiang, *Nature*, 2016, **532**, 85–89.
30 E. Contraires, J. Teisseire, E. Sondergard and E. Barthel, *Soft Matter*, 2016, **12**, 6067–6072.
31 T. Kim and K. Suh, *Soft Matter*, 2009, **5**, 4131–4135.
32 H. P. Greenspan, *J. Fluid Mech.*, 1978, **84**, 125–143.
33 M. K. Chaudhury and G. M. Whitesides, *Science*, 1992, **256**, 1539–1541.
34 C. Sun, X. W. Zhao, Y. H. Han and Z. Gu, *Thin Solid Films*, 2008, **516**, 4059–4063.
35 F. Lugli, G. Fioravanti, D. Pattini, L. Pasquali, M. Montecchi, D. Gentili, M. Murgia, Z. Hemmatian, M. Cavallini and F. Zerbetto, *Adv. Funct. Mater.*, 2013, **23**, 5543–5549.
36 B. Chandesris, U. Soupremanien and N. Dunoyer, *Colloids Surf., A*, 2013, **434**, 126–135.
37 O. Bliznyuk, H. P. Jansen, E. S. Kooij, H. J. Zandvliet and B. Poelsema, *Langmuir*, 2011, **27**, 11238–11245.
38 M. Zhang, L. Wang, Y. Hou, W. Shi, S. Feng and Y. Zheng, *Adv. Mater.*, 2015, **27**, 5057–5062.
39 B. Zhang, Q. Lei, Z. Wang and X. Zhang, *Langmuir*, 2016, **32**, 346–351.
40 S. Feng, S. Wang, C. Liu, Y. Zheng and Y. Hou, *Chem. Commun.*, 2015, **51**, 6010–6013.
41 J. Zhang and Y. Han, *Langmuir*, 2008, **24**, 796–801.
42 J. Li, Y. Hou, Y. Liu, C. Hao, M. Li, M. K. Chaudhury, S. Yao and Z. Wang, *Nat. Phys.*, 2016, **12**, 606–612.
43 C. Hao, Y. Liu, X. Chen, J. Li, M. Zhang, Y. Zhao and Z. Wang, *Small*, 2016, **12**, 1824.
44 H. Chen, P. Zhang, L. Zhang, H. Liu, Y. Jiang, D. Zhang, Z. Han and L. Jiang, *Nature*, 2016, **532**, 85–89.
45 Y. Lu, S. Sathasivam, J. Song, C. Crick, C. Carmalt and I. Parkin, *Science*, 2015, **347**, 1132–1135.
46 V. Jokinen, *Soft Matter*, 2016, **12**, 1100–1106.
47 J. Chung, J. Youngblood and C. Stafford, *Soft Matter*, 2007, **3**, 1163–1169.
48 H. Bai, X. Tian, Y. Zheng, J. Ju, Y. Zhao and L. Jiang, *Adv. Mater.*, 2010, **22**, 5521–5525.
49 E. Ueda, F. L. Geyer, V. Nedashkivska and P. A. Levkin, *Lab Chip*, 2012, **12**, 5218–5224.
50 M. J. Hancock, F. Yanagawa, Y. Jang, J. He, N. N. Kachouie, H. Kaji and A. Khademhosseini, *Small*, 2012, **8**, 393–403.
51 B. Chang, Q. Zhou, R. H. A. Ras, A. Shah, Z. G. Wu and K. Hjort, *Appl. Phys. Lett.*, 2016, **108**, 154102.
52 G. Piret, E. Galopin, Y. Coffinier, R. Boukherroub, D. Legrand and C. Slomianny, *Soft Matter*, 2011, **7**, 8642–8649.
53 E. Ueda and P. A. Levkin, *Adv. Mater.*, 2013, **25**, 1234–1247.
54 A. A. Popova, S. M. Schillo, K. Demir, E. Ueda, A. Nesterov-Mueller and P. A. Levkin, *Adv. Mater.*, 2015, **27**, 5217–5222.
55 F. L. Geyer, E. Ueda, U. Liebel, N. Grau and P. A. Levkin, *Angew. Chem., Int. Ed.*, 2011, **50**, 8424–8427.
56 A. N. Efremov, E. Stanganello, A. Welle, S. Scholpp and P. A. Levkin, *Biomaterials*, 2013, **34**, 1757–1763.
57 A. Ghosh, R. Ganguly, T. M. Schutzius and C. M. Megaridis, *Lab Chip*, 2014, **14**, 1538–1550.
58 B. Mondal, M. M. G. Eain, Q. Xu, V. M. Egan, J. Punch and A. M. Lyons, *ACS Appl. Mater. Interfaces*, 2015, **7**, 23575–23588.
59 P. S. Mahapatra, A. Ghosh, R. Ganguly and C. M. Megaridis, *Int. J. Heat Mass Transfer*, 2016, **92**, 877–883.
60 R. P. Garrod, L. G. Harris, W. C. Schofield, J. McGettrick, L. J. Ward, D. O. Teare and J. P. Badyal, *Langmuir*, 2007, **23**, 689–693.

61 V. Jokinen, L. Sainiemi and S. Franssila, *Adv. Mater.*, 2008, **20**, 3453–3456.
62 X. Zhang, H. Kono, Z. Liu, S. Nishimoto, D. A. Tryk, T. Murakami, H. Sakai, M. Abe and A. Fujishima, *Chem. Commun.*, 2007, 4949–4951.
63 H. Kinoshita, A. Ogasahara, Y. Fukuda and N. Ohmae, *Carbon*, 2010, **48**, 4403–4408.
64 J. Osicka, M. Ilcikova, A. Popelka, J. Filip, T. Bertok, J. Tkac and P. Kasak, *Langmuir*, 2016, **32**, 5491–5499.
65 D. Wu, J. Wang, S. Wu, Q. Chen, S. Zhao, H. Zhang, H. Sun and L. Jiang, *Adv. Funct. Mater.*, 2011, **21**, 2927–2932.
66 T. Xu, W. Shi, J. Huang, Y. Song, F. Zhang, L. Xu, X. Zhang and S. Wang, *ACS Nano*, 2017, **11**, 621–626.
67 W. Sun, S. Zhou, B. You and L. Wu, *J. Mater. Chem. A*, 2013, **1**, 3146–3154.
68 D. Wang, Y. Liu, X. Liu, F. Zhou, W. Liu and Q. Xue, *Chem. Commun.*, 2009, 7018–7020.
69 D. Wang, X. Wang, X. Liu and F. Zhou, *J. Phys. Chem. C*, 2010, **114**, 9938–9944.
70 Q. Xu, Y. Liu, F. Lin, B. Mondal and A. Lyons, *ACS Appl. Mater. Interfaces*, 2013, **5**, 8915–8924.
71 Y. Lai, Y. Tang, J. Gong, D. Gong, L. Chi, C. Lin and Z. Chen, *J. Mater. Chem.*, 2012, **22**, 7420–7426.
72 Y. Lai, J. Huang, Z. Cui, M. Ge, K. Zhang, Z. Chen and L. Chi, *Small*, 2016, **12**, 2203–2224.
73 K. Liu, M. Cao, A. Fujishima and L. Jiang, *Chem. Rev.*, 2014, **114**, 10044–10094.
74 S. J. Pastine, D. Okawa, B. Kessler, M. Rolandi, M. Llorente, A. Zettl and J. M. Frechet, *J. Am. Chem. Soc.*, 2008, **130**, 4238–4239.
75 Y. Lai, C. Lin, J. Huang, H. Zhuang, L. Sun and T. Nguyen, *Langmuir*, 2008, **24**, 3867–3873.
76 S. M. Kang, I. You, W. K. Cho, H. K. Shon, T. G. Lee, I. S. Choi, J. M. Karp and H. Lee, *Angew. Chem., Int. Ed.*, 2010, **49**, 9401–9404.
77 J. S. Li, E. Ueda, A. Nallapaneni, L. X. Li and P. A. Levkin, *Langmuir*, 2012, **28**, 8286–8291.
78 S. Zhao, H. Xia, D. Wu, C. Lv, Q. Chen, K. Ariga, L. Liu and H. Sun, *Soft Matter*, 2013, **9**, 4236–4240.
79 L. Sun, Y. Shi, B. Li, X. Li and Y. Wang, *Polym. Compos.*, 2013, **34**, 1076–1080.
80 S. Wang, T. Wang, P. Ge, P. Xue, S. Ye, H. Chen, Z. Li, J. Zhang and B. Yang, *Langmuir*, 2015, **31**, 4032–4039.
81 S. Daniel and M. Chaudhury, *Langmuir*, 2002, **18**, 3404–3407.
82 Y. Hou, S. Feng, L. Dai and Y. Zheng, *Chem. Mater.*, 2016, **28**, 3625–3629.
83 F. Brochard, *Langmuir*, 1989, **5**, 432–438.
84 P. G. de Gennes, *Rev. Mod. Phys.*, 1985, **57**, 827–863.
85 H. Suda and S. Yamada, *Langmuir*, 2003, **19**, 529–531.
86 A. Ghosh, R. Ganguly, T. M. Schutzius and C. M. Megaridis, *Lab Chip*, 2014, **14**, 1538–1550.

